An Investigation of Proposed Higher Order Effects in the Bruno-Vaynblat Model for Martensitic Phase Transformations

John Weatherwax, Dimitri Vaynblat, Oscar Bruno, and Ruben Rosales

September 18, 2004

Abstract

Static, extream pressure, phase transformations, such as thoes which occur when graphite transforms into diamond have been studied, both experimentally and theoretically, for a long time [11]. Relativly recently, experimental evidence began appearing that similar phase transformation also occur under extream dynamically induced pressures. In 2000 Oscar Bruno and Dimitri Vaynblat (BV) proposed a *zero parameter* a mathematical model that seems to capture extreamly well much of the quantitive and qualitative data available on these types of phase transformations [6, 7]. In the BV model a simplifying assumption involving "rarefaction discontinuities" was used along with a simple but typical, equation of state for the two phases. Consequently their results, while matching very well, dissagree slightly with experiment. In this paper we offer suggestions aimed at further improving the match of the BV theory with exeperiment. The improvements are further explained below but can be summarized as three main contributions that amount to 1) a mathematically correct treatment of rarefaction fans 2) an investigation of the effects of disapation to the mathematical model and 3) a study of improvements to the equations of state.

1 Introduction

Phase transitions are common in nature, such as the solid–to–liquid (melting) or liquid–to–gas (evaporation) changes most substances undergo as temperature and/or pressure are changed. Solid–to–solid phase transitions, while less common, also occur in nature. For example, the atomic structure of solid graphite can change to that of diamond under sufficiently large static pressures. These pressures are so large that they are difficult to achieve in static conditions, but they can easily be produced with shock waves. The jump in pressure carried by a strong shock wave can be large enough to promote the required atomic rearrangements. Small quantities of diamond can indeed be produced in this way [9, 12].

Shock–induced solid–to–solid phase transitions occur in systems other than the graphite–diamond one mentioned above. The α–iron to ϵ–iron phase transition discovered experimentally by Bancroft et al. in 1956 is another example. Bancroft et al. detected this phase transition by measuring the velocity of the free surface of an iron sample through which a strong shock wave passed [2].

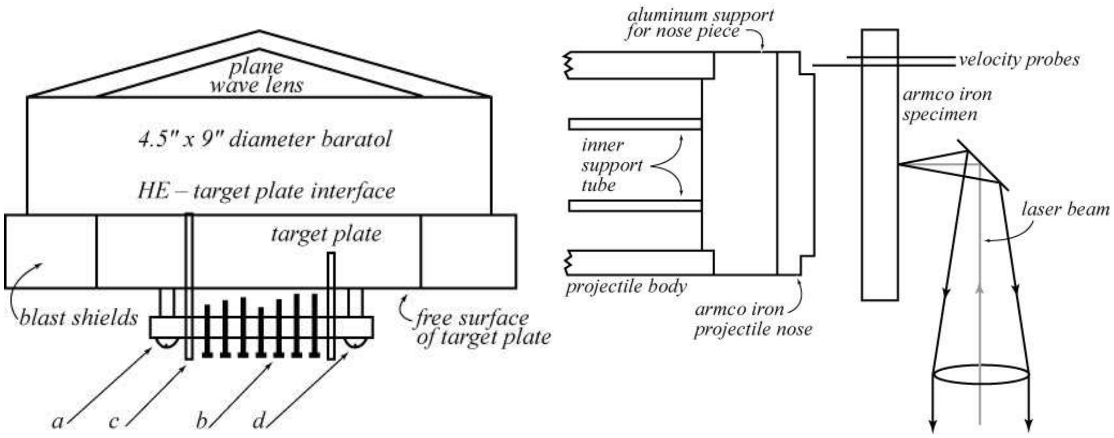

Figure 1: **Left:** Experimental apparatus used in the 1956 experiments by Bancroft et al. Letter **b** points to the series of pins. This picture is a replica of a similar one presented in [2]. **Right:** Setup for the Barker and Hollenbach experiments. The interferometer is not displayed. This picture is a replica of the one presented in [4].

In the experiment of Bancroft's, a shock wave in the iron sample was produced by an explosive charge (baratol) attached to one side of the sample under study. The surface opposite the charge was monitored by a series of electrical "pins", that sequentually shorted a monitoring circit as the free surface moved. The known spacing between consecutive pins and the measured time between electrical shorts enabled the experimenters to determine the velocity of the free surface as a function of time. Due to fundamental accuracy restrictions of the pin technique, extreamly accurate free surface velocity measurements, were not possible. See figure 1 for a schematic of the pin experimental technique.

Advances in laser interferometry technology allowed experiments of the same type as those carried by Bancroft et al., but with much more accurate measurements of the free surface velocity than was possible previously.

In 1974 Barker and Hollenbach performed impact experiments with an interferometer [4]. In figure 1 we show a schematic of the apparatus used to produce and record pressure waves in an input iron sample. The shock wave was generated by the impact of a driver, fired from a gas gun, into the sample. An interferometer situated on the opposite side of the sample was used to measure very accurately any deviations to the free surface. In figure 2 we show the experimental free surface profiles of several impacts corresponding to different inpactor velocities.

The accuracy of these experimental plots was great enough that theoratisians could begin to use them to compare against any developed theory. In 2000 Dimitri Vaynblat and Oscar Bruno developed a new theoretical model based on the mathematical theory of hyperbolic partial differential equations. This model is much simpler than previous theoretical discriptions and involves only well-known and separately measurable material constants [6, 7]. The Bruno–Vaynblat model, with a simplifying assumption they called the "rarefaction discontinuity approximation", gives qualitatively and quantitatively correct results for *both* the iron and the graphite-diamond experiments, see figure 2, for a comparison between the experimental profiles of Barker and Hollenbach and the theoretical predictions of the BV theory. In section 2 we provide a quick review of the Bruno–Vaynblat model, please see the papers [6, 7] for further details.

In *this* paper we revisit the BV model and further study the effects that each assumptions made has on the theoretically predicted experimental profiles. We begin by investigating the "rarefaction discontinuity" approximation. Recognizing that the BV model can be solved exactly (numerically) this is done and the results are compared with experiment. Second we in-

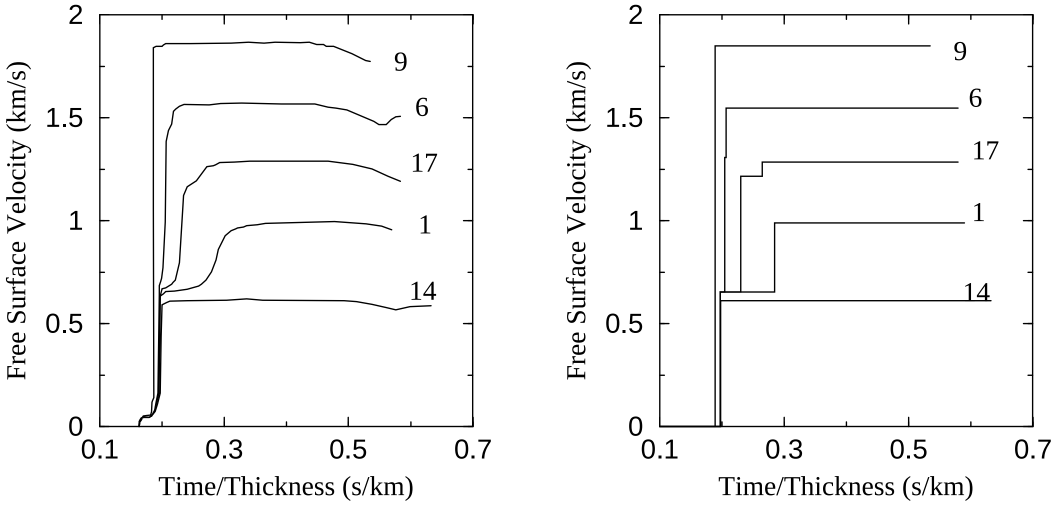

Figure 2: Free surface velocity profiles for the α-ϵ phase transition in shock loaded iron.
Left: Experimental measurements by Barker and Hollenbach [4].
Right: Bruno–Vaynblat theoretical model, using the "rarefaction discontinuity" approximation as found in [6].
Each curve represents a record of the free surface velocity for one experiment, with the numbers as assigned by Barker and Hollenbach to label their experiments. Only a few representative samples of their measurements are displayed in these plots. In terms of the impactor velocity, the curves order naturally from bottom (lowest velocity) to top (highest velocity), i.e.: as a function of increasing impactor velocity, the experiments are ordered in the sequence 14, 1, 17, 6, and 9.
The vertical axis is the free surface velocity and the horizontal axis is time scaled by the total thickness of the sample in each experiment.

vestigate the effect the addition of viscosity has on the predicted free surface profiles. Third and finally we consider modification to the equation of state (the relationship between pressure (P) and specific volumn (v) and how that modifies the predicted free surfaces. Each modification is consistant with the base BV theory and serves as additional exploration of the phenomina predicted.

2 Bruno–Vaynblat Theory

As mentioned in section 1, Bruno and Vaynblat proposed a new model for the shock induced martensitic phase transformations observed in impact experiments. Below we list the main assumptions implicitly or explicity stated in their model. Please see [6, 7, 24] for more information and additional details.

2.1 Fundamental Postulates

The Bruno–Vaynblat model is based on the following postulates:

1. Because the sample's thickness is so much smaller than its diameter, the problem can be formulated entirely in terms of one–dimensional wave propagation.
2. Because of the large pressures involved in the α-ϵ iron phase transformation (known to be around $\approx 10GPa$), the elastic properties of iron can be entirely neglected and only the plastic response of the material is important [11]. This means that the stress tensor can be taken as diagonal, and all the dynamic forcing attributed to a scalar "pressure" function p, so that the full equations of solid mechanics simplify greatly. These simplified equations turn out to have the same form as the equations governing a compressible fluid flow see [10].
3. There is good reason to believe that a relationship of the form $p = p(\mathrm{v})$ provides a good approximation to the behavior in each phase. Here p is the pressure and v is the specific volume. These empirical relationships will be denoted by $p^A(\mathrm{v})$ for austenitic phase and $p^M(\mathrm{v})$ for the martensitic phase.
4. The transformation among phases takes place at infinite speed, when some critical value of the pressure is reached. The critical pressures will be denoted by $p^A_{\text{crit}}(T)$ for the forward transformation and $p^M_{\text{crit}}(T)$ for the reverse transformation.

2.2 Mathematical Formulation

From assumptions 2 and 3 in subsection 2.1, the governing dynamical equations for the Bruno–Vaynblat model reduce to the conservation of mass and momentum [10]. In an Eulerian frame of reference these are

$$\frac{\partial}{\partial t}\rho + \frac{\partial}{\partial x}(\rho\, u) = 0\,, \qquad \text{and} \qquad \frac{\partial}{\partial t}(\rho\, u) + \frac{\partial}{\partial x}(\rho\, u^2 + p) = 0\,, \tag{1}$$

where ρ is the density, u is the particle velocity, p is the pressure, t is the time, and x is the Eulerian spatial position. An equivalent form, in a Lagrangian frame of reference is

$$\frac{\partial \mathrm{v}}{\partial t} - \frac{\partial u}{\partial \xi} = 0\,, \qquad \text{and} \qquad \frac{\partial u}{\partial t} + \frac{\partial p}{\partial \xi} = 0\,, \tag{2}$$

where $\mathrm{v} \equiv 1/\rho$ is the specific volume and ξ is the Lagrangian spatial coordinate, related to the Eulerian coordinate x by

$$\xi = \int_{x_0}^{x} \rho(\tilde{x}, t)\, \mathrm{d}\tilde{x}\,, \tag{3}$$

where $x_0 = x_0(t)$ is the Eulerian position of a fixed mass particle.

Here we will develop the theory in terms of the Eulerian coordinate system. A similar development, in terms of the Lagrangian coordinate system, can be found in the appendix in **??**.

From assumption number 4 of the Bruno-Vaynblat model (see subsection 2.1), the empirical pressure function $p = p(\mathrm{v})$ has the discontinuous form

$$p(\mathrm{v}) = \begin{cases} p^A(\mathrm{v}) & \text{for } p < p^A_{\text{crit}}\,, \\ p^M(\mathrm{v}) & \text{for } p > p^M_{\text{crit}}\,. \end{cases} \tag{4}$$

See figure **??** (a) for a graph of a typical equation of state used in **??**. As specified in the BV theory we assume from now on that both p^A_{crit} and p^M_{crit} are *known* constants. The specific equation of state used for either $p^A(\mathrm{v})$ or $p^M(\mathrm{v})$ are given by:

$$p(\eta) = \frac{\rho_0\, c_0^2\, \eta}{(1 - s\, \eta)^2}\,, \tag{5}$$

where η is defined by

$$\eta = 1 - \frac{\rho_0}{\rho} = 1 - \frac{\mathrm{v}}{\mathrm{v}_0}\,. \tag{6}$$

This form of the equation of state is known as a Mie-Grüneisen equation of state. The values of the coefficients selected are fully specified in Appendix **??**.

This equation of state is common in solid mechanics problems, for example see [?]. This paper will use 5 as a starting point for the calculations done here. In section **??** we discuss this equation of state and additional modifications to it.

When $p = p(\mathrm{v})$ is a convex smooth function with negative derivative, the system in (1) — equivalently, in (2) — is known as the *p-System*, and has been extensively studied in the mathematical literature, see [20]. In the Bruno–Vaynblat theory, because of the switch in the equation of state at the critical pressure, p is neither convex nor continuous, and further assumptions are needed to have a complete theory. The mathematical consequnces of this change in functional form of the equation of state are discussed fully in the references [6, 7]. The main consequences of this particulare equation of state over that of the p-System are that new waves called critical transformation are introduced into the Riemann problem. It will be assumed for this paper that the reader is familiar with the mathematical theory of hyperbolic equations and with the additional effects that a discontinus equation of state has on the Riemann problem.

2.3 Bruno–Vaynblat Results

In this section we will quickly summarize some of the main results obtained by Bruno and Vaynblat in their papers [6, 7]. What Bruno and Vaynblat did was to consider the initial impact of the driver and sample as a Riemann problem. Assuming an appropriate equation of state 4, equations of motion 2 and initial conditions given by:

$$p(x,0) = \begin{cases} p^l = 0 & \text{for } x < 0\,, \\ p^r = 0 & \text{for } x > 0\,, \end{cases} \quad \text{and} \quad u(x,0) = \begin{cases} u^l = u_{flyer} & \text{for } x < 0\,, \\ u^r = 0 & \text{for } x > 0\,. \end{cases} \tag{7}$$

With these components a mathematically closed system is obtained. We note that solving the Riemann problem associated with 2, 4 and initial conditions of 7 gives rise to only discontinuious waves. What Bruno and Vaynblat did at this point was to consider a simplification aimed at restricting all Riemann problems to result in discontinious waves. This approximation amounts to treating all rarefaction waves, produced from any Riemann problem, *not* as continious waves but as discontinuities. This approximation has been used for sometime in the solid mechanics community and amounts to what is know as the “rarefaction discontinuity approximation”. For comparisons further in this paper, in figure 3 we present a superposition of the experimental and theoretical predictions under the rarefaction discontinutiy approxmation.

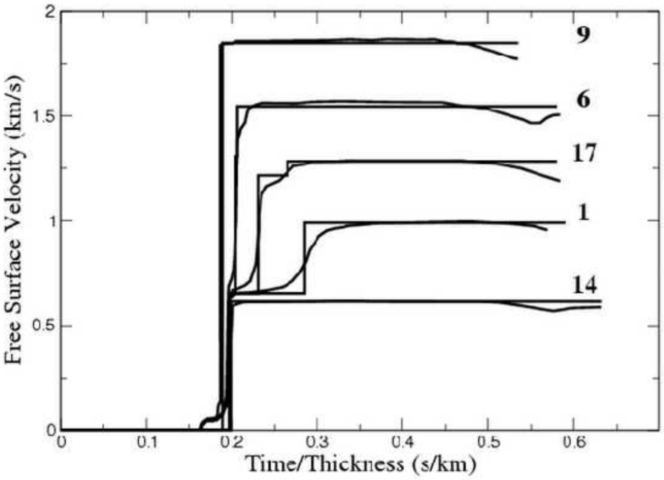

Figure 3: A superposition of the experimental and theoretical free surface velocities, under the rarefaction discontinuity approximation.

It is with this approximation that the plots produced in figure 2 and figure 3 were made.

Next we discuss observations about the experimental and theoretical plots and directions to head for additional improvements.

2.4 Dissagreements between the BV-Theory and Experiment

When one looks at the results obtained with the rarefaction discontinuity approximation, one cannot help but be amazed by the agreement with experiment. In these impact experiments the pressure jump the material experiences are on the order of $10^9\,Pa$. At these large pressures the rarefaction waves can hardly be considered weak. Thus it is entirely possible that the rarefaction wave approximation is loosing some important feature of the problem. Therefore, in the hopes of further improving the results of Bruno and Vaynblat, we concentrate on the qualitative *disagreements*, between their theoretical curves and the experimental ones. The observations made here will then form the basis for the modifications made by this author in later sections. In that direction, the two sets of curves, shown in figure 2 (page 4) differ in at least the following fundamental points:

- The rarefaction discontinuity approximation produces free surface velocity profiles that are "too steep". The experimental profiles numbered 1 and 17, have a steep, but *finite* slope (representing the increase in velocity achieved during the second wave). The predictions of the rarefaction discontinuity approximation, however, give infinite rise times for the second wave in each experiment. The experimental curve numbered 1 has the most shallow rise time for the second wave, and correspondingly the worst match with theory.

- The rarefaction discontinuity approximation produces corners that are "too sharp". The experimental profiles numbered 17 and 6 have smooth transitions between the jump accompanying the second wave and the limiting asymptotic velocity each assumes. The rarefaction discontinuity approximation, however, gives sharp angular corners at these locations on the graphs.

- For long times the rarefaction discontinuity approximation predicts a constant asymptotic value of free surface velocity. Many of the experimental curves have free surface velocities, however, are not constant for large values of time.

- The initial rise of the first wave in the rarefaction discontinuity plots are not prefixed by a tiny "toe" around the Time/Thickness of $0.2\, s/km$. In the experimental plots the first jump in free surface velocity is preceded by a relatively small jump before the Time/Thickness of $0.2\, s/km$, that is not present in the theoretical plots. It is believed that this "toe" is caused by the elastic responce of iron, while the remaining curves are produced by iron's plastic response **??**. As was done in the Bruno-Vaynblat papers it is only the waves propagation occurring in the *plastic* iron, that is modeled and all approximations made in the paper will neglect this toe.

The approach taken in this paper is to keep the basis of the Bruno-Vaynblat theory of martensitic phase transformations but to add new effects in a hope of removing some or all of the disagreements between the experimental and theoretical plots mentioned above. It is felt that the disagreement with respect to the slopes of the free surface plots, (first item mentioned), is the most important of all affects to try and capture. One obvious point that would need to be introduced into the theory if we are to hope for better agreement with regards to the smoothing of wave profiles is:

A smoothing effect had to be incorporated.

It seemed obvious that the first attempt at improving the model should be that of removing the rarefaction discontinutiy approximation and evaluating numerically the full equations.

To fully resolve the rarefaction fans, numerical schemes were implemented. These codes enabled the study, in a controlled environment, of the effects that including rarefaction fans have on the free surface velocity plots.

3 Full Bruno-Vaynblat Model, Including Fans

In this section we present predictions that the *full* Bruno-Vaynblat theory gives by including rarefaction fans in the different impact regimes corresponding to the experimental setups of Barker and Hollenbach [4]. The complete numerical flows, presented below, were constructed using two numerical schemes:

1. A Godunov type initial value solver.
2. A new numerical scheme, called the *Characterisitic Tracking Method*, developed in the course of working on this problem. The characteristic tracking method will be further discribed on its own in an additional paper see [23].

Both numerical schemes give the same results and we present all plots using the characteristic tracking method as it is much better at resolving the features of the flow. The qualitative predictions, presented here, are illustrated with figures which resulted from numerical simulations, utilizing actual material constants — obtained as indicated in Appendix **??**.

In figure 4 we see a plot similar to figure 2 with rarefaction fans included. The first natural thing to notice is that the improvement in free surface profiles, especially with respect to profile number 1, is slight. The reason for the limited improvement will be explained below. It is however interesting to remark that these plots here involve *no* adjustable parameters. They are the results of a fully consistant zero parameter mathematical model discribing martensitic phase transformations. It is remarkable that the power of capturing the phenomina lies inherently in the Bruno-Vaynblat critical pressure hypothesis and the underlying mathematics of the resulting hyperbolic system.

We note here that due to lack of space we will focus soley on the physical aspect of the problem, seeking additional effects that will hopefully result in an even more realistic free surface profiles. In having this emphasis we will be forced to ignore most of the interesting mathematics involving the interactions of compressive and expansive simple waves under the Bruno-Vaynblat model. Readers interested in these topics are advised to consider the following references [6, 7, 24].

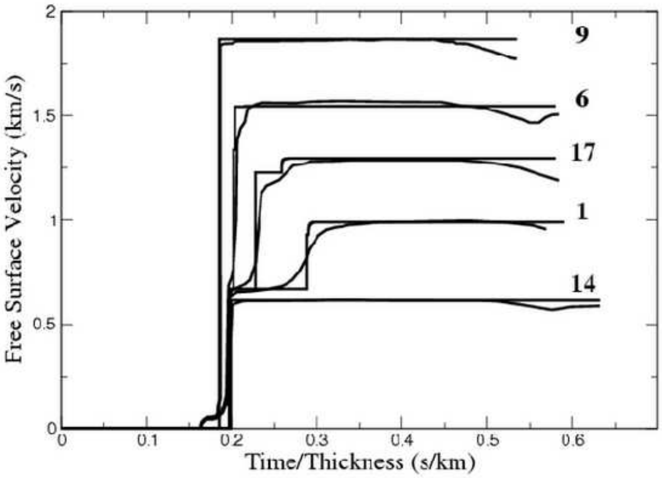

Figure 4: Experimental and theoretical free surface velocity profiles for the α-ϵ phase transition in shock loaded iron under the *complete* Bruno Vaynblat experimental model. We note that in profiles 1 and 17 the inclusion of rarefaction fans *has* rounded the corners of the free surface velocity plots some but much of the vertical structure we were trying to elliminate still remains.

4 Additional Physical Effects

The results and dynamics of including rarefaction fans into the numerics are presented in section 3. The inclusion of rarefaction fans into the Bruno-

Vaynblat model gave *somewhat* smoother free surface profiles. It seems that we learn that the smoothing effect of rarefaction fans are not enough to drastically affect the free surface profiles and in order to further improve the theory, additional smoothing of some form is needed. Three physical effects currently neglected and that would smooth this compressive simple wave are considered.

1. Internal dissipation maybe important. Generically there is always dissipation, and this energy loss needs to be included in the model. Incorrectly modeling phase transformations as energy conserving, by not including dissipation, could result in pictures of qualitatively the same type as presented in figure 4. This investigation is reported on in section 5.

2. The equation of state of austenite, while well known for pressures far from critical, cannot be claimed to be known accurately for pressures near or close to critical. We exploit this fact by modifying the austenitic equation of state near the critical transformation pressure for austenite. This modification while more indirect than other methods can lead to smoother free surface profiles. This investigation is reported on in chapter **??** section 7.

3. As discussed in section **??**, an alternate approach to the theory of austenitic-martensitic phase transitions is based on the idea of a relaxation time. These effects have been incorporated in past models, see for instance [5, 22]. In some cases it is found that, to achieve good agreement with experiment, a different relaxation time is required for each experimental curve, which is not a very satisfactory situation [5]. Since several previous theoretical studies have investigated this effect, we focused the efforts of this work on the previous two ideas. Plans to incorporate the relaxation idea into the Bruno-Vaynblat model exist and the results of this investigation are planned for another paper.

The next section is concerned with the implementations of several of the ideas discussed here. We begin by considering the effect dissipation has on the full Bruno-Vaynblat model and then look at modifications to the austenitic equation of state.

5 Dissipative Effects

In this section we will study the importance and effects of dissipation in the shock induced phase transitions under consideration. First we will give arguments indicating why dissipation may be important, then we will modify the model equations to include dissipation in as simple a way as possible, next we will introduce a numerical scheme to solve the modified equations, and finally we will analyze the results from this modification.

5.1 Motivation

In this subsection we give some arguments indicating that the amount of dissipation, in the regime of the shock induced phase transitions we consider, may be quite large — so that it should not be neglected. These arguments will be used as a motivation for including dissipation into the governing equations in (2), followed by an investigation of the effect this has on the predictions of the model.

We begin by pointing out that, after each flyer-plate experiment is finished, the target material is completely destroyed. Therefore, measurements can only be taken of the free surface for a very short time (while the target is still in one piece). Furthermore: a full explanation of what happens internally in the target (causing its destruction) is not known.

A hint at the motivation for the addition of viscosity can be seen by looking at the x-t diagrams corresponding to regime B impacts (see references [24, **?**]). A possible explanation (for the destruction of the sample) is the following: When the precursor shock propagates through the target, it raises the sample pressure/stress from atmospheric to critical. Thus, a region of critical austenite forms between the precursor shock and the phase transition front (traveling behind the shock, at a slower velocity). One may ask then: what keeps the austenite in the critical region from changing phase right after the shock passes, and forces it to wait till the phase transition front arrives? The explanation for this is, roughly, as follows: In iron the martensite phase has a volume contraction of about 20%, relative to the volume of the austenite phase. Such contraction cannot happen at some arbitrary place inside the material, for the volume reduction would immediately make the pressure drop below critical (stopping the phase change). Thus, the austenite must wait till the phase transition front (which, effectively, carries the volume reduction needed for the transformation) arrives, before it can change into martensite.

There is, however, a catch to the explanation at the end of the last paragraph. Namely: it only makes sense for an ideal material, with no defects of any kind. The reason is that defects allow the contraction needed to happen, at the price of a fracture in the target material. Further, any such fracture will (generally) allow more fractures to happen, the net consequence of this being that very many fractures will develop in the target (in the region between the precursor shock and the transition front), with some amount of phase transition occurring before the arrival of the main phase transformation front. These fractures are then the cause of the sample destruction.

Modeling at the "continuum" level of the process described in the prior paragraph is very hard, and beyond our current level of understanding — in fact, trying to avoid such modeling was one of the main motivations Bruno and Vaynblat had when they developed their model. We will not attempt to do this here, but we observe that one important consequence of this process is that we can expect a large amount of dissipation to occur because of it: From the view point of the transformation wave, the cracked material it travels through is extremely dissipative. Thus we propose to include dissipation into the model, and do so in as simple a way as possible. Namely: we will take an approach similar to the one that is used in the modeling of dissipation by turbulent fluid flows, and add an "effective" viscosity to the governing equations — note that this viscosity is not molecular viscosity, which is usually quite small, in fact, we expect it to be large. This "viscosity" will, unfortunately, be a free parameter (which we do not know how to measure independently). Actually, in agreement with the motivation for this dissipative model, we will introduce two viscosities, namely: one value will apply ahead of the precursor shock, and a second (much larger one) behind it.

We note that this work here is the first to incorporate the idea of an effective viscosity within the context of phase transformations. It is the very fact that the Bruno–Vaynblat model excludes mixture regions that allows us to treat both the effects of viscosity and phase transformation within the context of the same model. Previous authors have used the idea of an effective viscosity to study the dislocation density in a material [15], and (from this point of view) our viscosity approach can be stated as postulating an increase in the dislocation density as the result of the precursor shock raising the pressure to critical.

An important point to be made here, is that *the introduced dissipation* *does not affect the thickness of the transformation front itself.* Thus, in our modified model the shocks will no longer be modeled as discontinuities, but the transformation fronts will still be discontinuous — see figure 5. As mentioned in a previous paragraph the knowledge of how to incorporate viscous flow and phase transitions under a continioum theory is beyond the current state of understanding, thus we sweep this problem “under the rug” and place viscosity in the regions on either side of the phase transformation.

Notice that the main effect of introducing dissipation into a hyperbolic system is the “smearing” of the shocks, and the widening of the rarefaction fans (see reference [25]). This, clearly, will tend to make the theoretical free surface plots more like the experimental ones.

5.2 Dissipative Governing Equations

We modify the Eulerian equations (1), to include dissipation, as follows:

$$\frac{\partial}{\partial t}\rho + \frac{\partial}{\partial x}(\rho\, u) = 0\,, \qquad \frac{\partial}{\partial t}(\rho\, u) + \frac{\partial}{\partial x}(\rho\, u^2 + p) = \mu\, \frac{\partial^2}{\partial x^2}u\,, \tag{8}$$

where the viscosity coefficient μ is a measure of the amount of dissipation present in the system. Equivalently, the Lagrangian equations (2) become

$$\frac{\partial}{\partial t}\mathrm{v} - \frac{\partial}{\partial \xi}\mathrm{u} = 0\,, \qquad \frac{\partial}{\partial \mathrm{t}}\mathrm{u} + \frac{\partial}{\partial \xi}\mathrm{p} = \mu\, \frac{\partial}{\partial \xi}\left(\frac{1}{\mathrm{v}}\frac{\partial \mathrm{u}}{\partial \xi}\right)\,. \tag{9}$$

To study the effect that the added viscous term has on the free surface plots, we solved numerically the Lagrangian equations in (9). In what follows we will first present a brief discussion of the numerical algorithm used in solving these equations, followed by a presentation of some selected results from the numerical calculations, and finally comment on the results obtained.

We note that these equations are more complicated than they appear upon a cursory examination. The problem appears because of the phase transitions, across which the equation of state (relating the pressure p to the density ρ) has a discontinuity. This introduces discontinuities in the flow variables, which makes the meaning of the twice-differentiated dissipative term not clear at the location of the phase transitions. We will deal with this difficulty in what follows, within the context of the numerical algorithm.

6 Dissipative Numerics

In this section we describe the motivation and discretizations used in the numerical algorithm chosen for this problem. In section 4 of chapter **??**, we discussed several qualitative differences between the free surface velocity plots generated using the Bruno–Vaynblat model and the experimental measurements of Barker and Hollenbach. Of the differences noted, the most important disagreement was in the slope (or width) of the second wave. All the theoretical free surface predictions (thus far) have slopes that are almost vertical, while the experimental curves are much smoother. The greatest disagreement in regards to this effect, occurs with the first experiment presented in Barker and Hollenbach [4]. This experiment corresponds to a parameter regime B impact (see subsection **??**). Thus, the numerical scheme is implemented with the aim of solving the equations in (9) for regime B impacts.

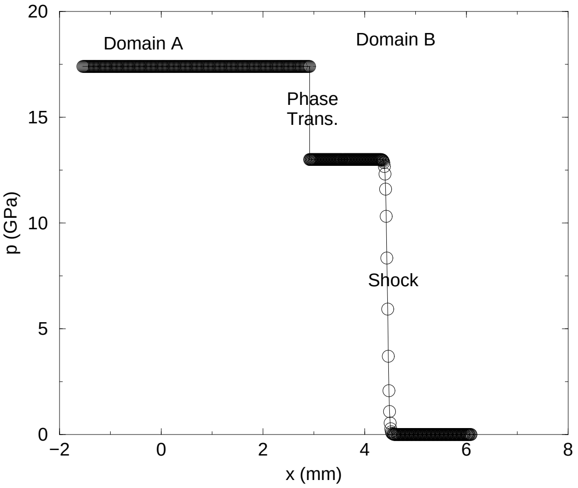

Figure 5: Hypothetical diffusive pressure wave profile, for an impact in the parameter regime B, plotted at a time shortly after the impact. The horizontal axis is distance, in millimeters, measured from the point of impact. The vertical axis is pressure, in Giga Pascals. Domain A (respectively B) is defined as all the points to the left (respectively, to the right) of the phase transformation. Here we see the right-facing phase transformation, present as a discontinuity, and the right-facing shock, slightly smeared by the viscosity, both propagating towards the free surface — located at $x \approx 6\,mm$.

For regime B impacts, the first Riemann problem (between the flyer and the target) produces two right-facing waves: a precursor shock and a phase transformation, see figure **??**. A hypothetical representation of the solution at a time after impact, but before the precursor shock has collided with the free surface, is shown in figure 5. There one can see the precursor shock broadened by the dissipation: the shock is now a compression wave where the competing effects of nonlinearity and diffusion balance each other. It is clear from this figure that the phase transformation front divides the material into *two domains of interest: domain A* (containing martensite, behind the transformation front) and *domain B* (containing austenite, ahead of the transformation front).

The natural division of the flow into separate domains, by a moving phase transformation discontinuity, is what motivates the transformation given below — in which we consider a general case, with more than one discontinuity and more than two domains. Specifically, we derive discrete numerical equations for M domains, separated by $M+1$ interfaces — including the left end of the first domain, and the right end of the last domain (that is: the left and the right ends of the sample, respectively). *In each domain there is a single phase, either austenite or martensite, so that a single equation of state applies.* Thus, in each domain the equations in (9) have a clear meaning, and standard finite difference discretizations can be used. The problem is then reduced to the question of how to solve the equations across the phase transition fronts, where the equation of state has a discontinuous jump, and the meaning of the equations in (9) has to be clarified.

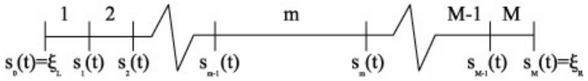

Figure 6: Several domains separated by moving discontinuities, including the left end of the first domain and the right end of the last domain — that is: the left and the right sample ends, respectively. Each discontinuity is a phase transition, and in each domain there is a constant phase, either austenite or martensite.

Consider a section of the real line from ξ_L to ξ_R, containing $M+1$ interfaces and M domains, as in figure 6. Assume that, as a function of time t, the locations of the interfaces are given by the smooth functions $\xi = s_i(t)$, where $0 \le i \le M$, $\xi_L = s_0(t)$ corresponds to the left end of the sample, and $\xi_R = s_M(t)$ corresponds to the right end. Notice that we work in Lagrangian coordinates, where the function $\xi = s_i(t)$ indicates the mass to the left of the given interface (up to some constant, generally selected so that $\xi_L = 0$), and $\mathcal{M}_i = \dot{s}_i(t)$ is the mass flux across the interface. A similar formulation is possible in Eulerian coordinates, where the values $s_i(t)$ and $\dot{s}_i(t)$ give the location in space and velocity of the i-th interface.

In any given domain ($s_{m-1}(t) \le \xi \le s_m(t)$), define the coordinate transformation $\xi \to \xi_m$ by

$$\xi_m = \frac{\xi - s_{m-1}(t)}{s_m(t) - s_{m-1}(t)}\,, \qquad \text{so that} \qquad \begin{cases} \xi = s_{m-1} & \Longleftrightarrow \quad \xi_m = 0\,. \\ \xi = s_m & \Longleftrightarrow \quad \xi_m = 1\,. \end{cases} \tag{10}$$

Thus the m-th domain is transformed into the fixed interval $[0, 1]$ — this is a mathematical trick often used in free surface calculations [13]. Of course, the functions $s_i(t)$ are not known beforehand, so that the price we pay for simplifying the domain of integration (eliminating the free surfaces) is to introduce a new unknown for each domain — namely: the functions $s_m(t)$, $1 \le m \le M$.

In each domain, we can now write the equations in (9) in terms of the local variable ξ_m, using equation (10) above. Conservation of mass, the first equation in (9), becomes

$$\frac{\partial}{\partial t}\mathrm{v} - \frac{1}{\mathrm{s_m - s_{m-1}}}\left[\left((1-\xi)\,\dot{\mathrm{s}}_{\mathrm{m-1}} + \xi\,\dot{\mathrm{s}}_{\mathrm{m}}\right)\frac{\partial}{\partial \xi}\mathrm{v} + \frac{\partial}{\partial \xi}\mathrm{u}\right] = 0\,, \tag{11}$$

and conservation of momentum, the second equation in (9), becomes

$$\frac{\partial}{\partial t}u - \frac{(1-\xi)\,\dot{s}_{m-1} + \xi\,\dot{s}_m}{s_m - s_{m-1}}\,\frac{\partial}{\partial \xi}u + \frac{1}{s_m - s_{m-1}}\,\frac{\partial}{\partial \xi}p = \frac{\mu}{(s_m - s_{m-1})^2}\,\frac{\partial}{\partial \xi}\left(\frac{1}{\mathrm{v}}\frac{\partial u}{\partial \xi}\right)\,, \tag{12}$$

where, to simplify the notation, we have dropped the subscript m on ξ_m. Next we discretize these equations, using a finite differences staggered grid approach.

Break up each domain $0 \le \xi \le 1$ into a uniform grid, with N nodes, including the end points. Namely, let

$$\xi_i = (i-1)\,\Delta\xi\,, \qquad \text{where} \quad \Delta\xi = \frac{1}{N-1} \quad \text{and} \quad 1 \le i \le N\,, \tag{13}$$

be the *nodes*, and call the interval $\xi_i \le \xi \le \xi_{i+1}$ the *i-th cell* — with *center:* $\xi_{i+\frac{1}{2}} = \frac{1}{2}\,(\xi_i + \xi_{i+1})$. Then, for the specific volume v (and density $\rho = 1/\mathrm{v}$) we use a node centered approach, with the numerical scheme carrying the values of the density at the nodes — i.e., the values: $\mathrm{v}(\xi_\mathrm{i}, \mathrm{t})$. For the velocity, on the other hand, we use a cell centered approach, with the numerical scheme carrying the values of the velocity at the cell centers — i.e., the values: $u(\xi_{i+\frac{1}{2}}, t)$. It is now convenient to introduce *notation to denote whether a numerical variable is defined on nodes or cells.* To be specific, when referring to a cell centered variable, for example u, we will use a bar, as in $\bar{u}$. On the other hand, a node centered variable will receive no special indication. Thus the notation v_ξ applies to the node centered value of the ξ derivative of the specific volume, while $\bar{\mathrm{v}}_\xi$ means the cell centered value of the same thing. With these definitions we are now in a position to write down the spatial discretization of the dissipative equations in (11) and (12) are, using the staggered grid technique, as done in the subsections that follow.

We point out that the *full* discretization of the equations in (11) and (12) will be done using the *method of lines.* In this method one first discretizes the spatial derivatives, forming a semi-discrete system of equations, and then uses an ordinary differential equation solver to discretize the time derivatives. Following this approach, in the presentation below we first focus on obtaining semi-discrete approximations to the governing partial differential equations, and afterwards deal with the discretization of the time derivatives, so as to obtain a fully discrete set of equations.

6.1 Method of Lines Applied to the Dissipative Problem

Since the method of lines applied to the equation in (11), representing conservation of mass, involves updating a node centered variable, v, we need discrete versions for the spatial derivatives in the equation, centered at the nodes. Thus we use centered differences to approximate the spatial derivatives appearing in equation (11), namely:

$$\frac{\partial}{\partial \xi}\mathrm{v}(\xi_\mathrm{i}, \mathrm{t}) \approx \frac{\mathrm{v}(\xi_{\mathrm{i}+1}, \mathrm{t}) - \mathrm{v}(\xi_{\mathrm{i}-1}, \mathrm{t})}{2\Delta\xi} \qquad \text{and} \qquad \frac{\partial}{\partial \xi}\mathrm{u}(\xi_\mathrm{i}, \mathrm{t}) \approx \frac{\bar{\mathrm{u}}(\xi_{\mathrm{i}+\frac{1}{2}}, \mathrm{t}) - \bar{\mathrm{u}}(\xi_{\mathrm{i}-\frac{1}{2}}, \mathrm{t})}{\Delta\xi}, \tag{14}$$

where we note that both expressions on the right hand side involve the natural domain of definition of the variables involved (node centered densities and cell centered velocities). These approximations, when used in (11), lead to the following semi-discrete system (correct up to second order in $\Delta\xi$) for the conservation of mass

$$\begin{aligned} \frac{\partial}{\partial t}\mathrm{v}(\xi_{\mathrm{i}},\mathrm{t}) &= \left(\frac{(1-\xi_i)\,\dot{s}_{m-1}+\xi_i\,\dot{s}_m}{s_m-s_{m-1}}\right)\frac{\mathrm{v}(\xi_{\mathrm{i+1}},\mathrm{t})-\mathrm{v}(\xi_{\mathrm{i-1}},\mathrm{t})}{2\,\Delta\xi} \\ &+ \left(\frac{1}{s_m-s_{m-1}}\right)\frac{\bar{u}(\xi_{i+\frac{1}{2}},t)-\bar{u}(\xi_{i-\frac{1}{2}},t)}{\Delta\xi}\,. \end{aligned} \tag{15}$$

A similar process can be applied to the equation in (12), for the conservation of momentum. This requires updating (in time) the velocity, a cell centered variable, so that cell centered approximations for the various derivatives with respect to ξ involved are needed. The exact discretizations selected to do this are no more technically complicated than the ones used above in the conservation of mass equation, but contain more terms. Thus, to avoid displaying long formulas here, the semi-discrete equations for the conservation of momentum are shown in appendix **??**.

The discretizations above are, of course, valid only inside each domain — where the relationship between p and v, as given by the equation of state, is smooth. We need now to worry about what happens at the ends of each domain, where two type of situations may arise: either the end of the domain coincides with the end of the sample (i.e.: s_i for $i = 0$ or $i = M$), or the end of the domain corresponds to the location of a phase transition (i.e.: s_i for $0 < i < M$). This leads to two types of boundary conditions, that must be imposed at the domain ends, which we call (respectively) *outer boundary conditions* and *inner boundary conditions.* We note that, in order *to consider the resolution of this problem, we can restrict the discussion to the simpler case* $M = 2$*,* when there are only two domains — such as in the example shown in figure 5 for a typical initial condition in the parameter regime B, where a single right-moving, discontinuous, phase transformation front separates the martensite on the left from the austenite on the right. In this case, as indicated in the figure caption, we will call the martensite domain the domain A, and the austenite domain the domain B — note that the precursor shock wave in the austenite is not a true discontinuity in the dissipative approximation, and it is not a domain boundary.

In the numerical calculations we are not interested in computing for times large enough that wave reflections from the back end of the impactor reach the free surface. In the particular case of two domains, such as the one in figure 5, this means that we can *assume that the left boundary of domain A is at negative infinity* — with the right boundary at the phase transformation, located at $s(t)$. On the other hand, domain B is bounded on its left by the phase transformation front, and on its right by the free surface, at ξ_R. Finally, we note that, as the flow evolves, the phase transformation wave will change type: from a right moving phase transformation front, to a contact discontinuity, to a left moving phase transformation front — see subsection **??**. Thus the domain boundaries are not always phase transformation fronts, and can even switch from being one to being a contact discontinuities, or vice versa. *Generally, the domain boundaries are just discontinuities (or interfaces), separating the martensite phase on one side from the austenite phase on the other.*

Going back to the issue of the boundary conditions, we note that the discretizations for the conservation of mass and momentum equations in (15) and (**??**)), both require information about the specific volume and the velocity one node and one cell away from the cell or node on which the time derivative terms in the semi-discrete equation are centered. Thus these equations cannot be used sufficiently close to a boundary. In the next subsection we discuss the additional equations used to solve for the nodes and cells near boundaries (the inner and outer boundary conditions mentioned earlier in this subsection).

6.2 Boundary Conditions

In this subsection we discuss the equations used to update the unknowns, for nodes and cells, near the numerical domain boundaries. Two different types of boundary conditions are discussed here. The first type, which we call the *outer boundary conditions*, apply at the ends of the computational domain, namely: at ξ_L and ξ_R. The second type, which we call the *inner boundary conditions*, are the conditions needed at the interfaces between the domains. The exact conditions used at any given interface depend on the type of discontinuity separating the domains, be it a forward transformation front, a contact discontinuity, or a backwards transformation front. Below we discuss these two types of boundary conditions, as used in the numerical simulations.

6.2.1 Outer Boundary Conditions

The stencils of the semi-discrete equations, in (15) and (**??**), require the specification of variables one node and one cell to either side of the node or the cell at the stencil center. As a consequence of this fact, two boundary conditions are required on each outer boundary. This is consistent with the increase in order of the model partial differential equations, due to the added dissipative term.

To model numerically the semi-infinite nature of domain A, we argue that: for a sufficiently large and negative value of ξ, the specific volume should be constant. Thus we set $\mathrm{v} = \mathrm{v_L}$ at $\xi = \xi_L$, where $\mathrm{v_L}$ is obtained from the solution of the first Riemann problem (the collision of the impactor and the flyer), a calculation that is done before the full viscous flow computation is started. This gives one of the two boundary conditions needed on the left end of the numerical domain.

Similarly, we argue that on the right end of domain B the specific volume should also be a constant, i.e.: $\mathrm{v} = \mathrm{v_R}$ on ξ_R, where the constant is determined by the equation $p(\mathrm{v_R}) = 0$. This follows because the right boundary of domain B is a free surface, and cannot support any pressure.

Finally, to determine the second boundary condition required at each end, we use the conservation of mass equation in (9). From this equation it is clear that, if v is constant along a particle path $\xi =$ constant, it follows that

$$\frac{\partial}{\partial \xi} u = 0\,. \tag{16}$$

This gives a second boundary condition, applicable on any $\xi =$ constant boundary, where v is kept constant.

6.2.2 Inner Boundary Conditions

Here we will formulate the boundary conditions used at the interface between the two domains, A and B, across which there is a jump in the equation of state (martensite on one side and austenite on the other). First we will consider all the unknowns/variables (at or near the interface) that cannot be updated by either of the equations in (15) or (**??**), and then we will systematically provide the extra equations needed to update their values.

We begin by considering the immediate neighborhood of the interface, and the associated unknowns there. Figure 7 shows a schematic representation of the situation. In this figure the interface is denoted with a cross, the nodes with solid dots and the cell centers with open dots. There are, however, some *important clarifications that must must be made with regard with this figure:* in fact, the rightmost node of the left domain (node N in the figure), the leftmost node of the right domain (node 1 in the figure), and the interface are the same point in space, but we have represented them separately in the picture — because they play different roles in the numerical algorithm. Similarly, there is no cell N belonging to the left domain, nor is there a cell 0 belonging to the right domain, but (for numerical reasons, which will become clear in the development that follows below) these *ghost cells* have been introduced in the figure. We note that, in space, the N-th (ghost) cell of the left domain is actually to the right of the interface — it represents a ghost extension of the state of the material phase on the left of the interface, to the right of the interface. Similarly, in space, the 0-th (ghost) cell of the right domain is actually to the left of the interface.

Figure 7: Schematic representation of the numerical grid near an interface. The interface is indicated by a cross, the nodes by solid dots and the cell centers by open dots. We note that, in fact, the rightmost node (i.e.: N) of the left domain, the leftmost node (i.e.: 1) of the right domain, and the interface are the same point in space, but (because they play different roles in the numerical algorithm) they are represented separately in the picture. Similarly, there is no cell N belonging to the left domain, nor is there a cell 0 belonging to the right domain, but (for reasons, explained in the text) these *ghost cells* are introduced by the numerical algorithm — they represent extensions of the material phases on each side of the interface, to the other side. In space, the N-th (ghost) cell of the left domain is actually to the right of the interface, and the 0-th (ghost) cell of the right domain is actually to the left of the interface.

The representation of the numerical grid shown in figure 7 provides a convenient way to label the unknowns around the interface. In this representation, each node and cell center carries one unknown (the values of the specific volume and velocity, respectively) and the interface carries two unknowns, namely: its Lagrangian coordinate position $\xi = s(t)$, and the mass flow across the interface $\mathcal{M} = \dot{s}$ — both as introduced by the transformation in (10), mapping the equations to a fixed $[0, 1]$ grid.

To update (in time) the specific volume in the node labeled $N - 1$, the formula in equation (15) can be used, since an additional cell and node exist to either side of this node. The same statement can be made about the cell center labeled $N - 1$, using the formula in equation (**??**). Similarly, the cell center labeled 1, and the node labeled 2, can be updated using the semi-discrete formulas in (15) and (**??**). This still leaves six variables for which the regular stencil used in the semi–discrete equations cannot be used, and for which extra equations are needed. These are:

$$\mathrm{v}_{\mathrm{N}}\,, \quad \bar{\mathrm{u}}_{\mathrm{N}}\,, \quad \mathrm{s}\,, \quad \dot{\mathrm{s}}\,, \quad \bar{\mathrm{u}}_0\,, \quad \text{and} \quad \mathrm{v}_1\,.$$

The first extra equation is obtained by approximating the mass flux through the interface (i.e.: $\mathcal{M} = \dot{s}$) by the finite difference formula

$$\dot{s} \approx \frac{s^{n+1} - s^n}{\Delta t}\,, \tag{17}$$

where s^n is the value of $s = s(t)$ at time $t = t_n$, and $\Delta t = t_{n+1} - t_n$ (higher order approximations for the time derivative are also possible, of course, but this is the one that we used). The other five extra equations will depend on the type of interface between the two domains. They are presented in detail below in their continuous forms, and in their discretized forms in appendix **??**. In summary: two equations follow from the Rankine-Hugoniot jump conditions (conservation of mass and momentum across the interface), one equation from knowledge of the specific interface type, and the remaining two equations are obtained from a numerical extrapolation process to be described below. There are now two cases to consider, depending on the interface type.

Case 1: the interface is a forward or backwards transformation front.

Two of the equations follow from the conservation of mass and momentum across the interface, where care must be taken to include the fluxes due to the dissipative terms. Modifying the equations in (**??**) to include the fluxes due to dissipation, we get

$$\dot{s}\,[\mathrm{v}] + [\mathrm{u}] = 0 \qquad \text{and} \qquad \dot{\mathrm{s}}\,[\mathrm{u}] - \left[\mathrm{p}(\mathrm{v}) - \frac{\mu}{\mathrm{v}}\frac{\partial}{\partial \xi}\mathrm{u}\right] = 0\,, \tag{18}$$

where the partial derivative u_ξ must be computed without crossing the discontinuity — it is because of the need to compute this derivative that the ghost cells were introduced earlier. We note that, in order to derive these equations, we have assumed that *there is no viscous contribution to the momentum flux arising from the phase transformation.* Mathematically this means that singularities of order higher than Dirac deltas are ignored. These singularities arise from the dissipative term in (9), because the variables are discontinuous across the interface. After this is done, the second jump condition above in (18) guarantees the cancellation of the remaining distribution (Dirac's deltas) part in the momentum equation in (9).

A further condition, that is specific to transformation fronts (forward and backwards), follows from the fact that the pressure ahead of the wave must be at the critical value for the phase that the wave is propagating into. This gives a third equation

$$p_N = p_{\text{crit}}^{\{A,M\}} \qquad \text{or} \qquad p_1 = p_{\text{crit}}^{\{A,M\}}\,, \tag{19}$$

where which formula is used depends on the direction of propagation of the interface, and the type of phase transformation.

Finally, the two remaining boundary conditions are obtained from a numerical approximation. As explained above, the ghost cells are introduced because of the need to compute the derivatives u_ξ in the right equation in (18). However, this is meaningless unless values for the velocities are provided at the ghost cell centers. A reasonable approach to doing this is to use extrapolation of the values of the velocity, from the side the ghost cell belongs to. We found, through experimentation with various possibilities, that first order extrapolation gives reasonable results for this purpose. This yields, on the uniform grids we used (see (13)), the following equations for $\bar{u}_N$ and $\bar{u}_0$

$$\bar{u}_0 = 2\,\bar{u}_1 + \bar{u}_2 \qquad \text{and} \qquad \bar{u}_N = 2\,\bar{u}_{N-1} + \bar{u}_{N-2}\,. \tag{20}$$

Case 2: the interface is a contact discontinuity.
In this case

$$\frac{ds}{dt} = 0\,, \tag{21}$$

because no mass crosses the interface. This gives a condition specific to contact discontinuities only. Conservation of mass and momentum now take the simpler forms

$$[u] = 0 \qquad \text{and} \qquad \left[p(\mathrm{v}) - \frac{\mu}{\mathrm{v}}\frac{\partial}{\partial \xi}\mathrm{u}\right] = 0\,, \tag{22}$$

where the same remarks made after the equations in (18) apply. Finally, two additional (numerical) boundary conditions are obtained by manipulation of the conservation of mass differential equation in (11). This equation yields, when evaluated on the N-th node:

$$\frac{d}{dt}\mathrm{v}_{\mathrm{N}} - \frac{1}{\mathrm{s} - \xi_{\mathrm{L}}}\frac{\partial}{\partial \xi}\mathrm{u}_{\mathrm{N}} = 0\,,$$

where we have used the fact that we have only two domains, that the node is actually a particle path, and that $\dot{s} = 0$. A semi-discrete equation for v_{N} can now be obtained by discretizing the spatial derivative of the velocity in this equation, using finite differences. This gives

$$\frac{d}{dt}\mathrm{v}_{\mathrm{N}} - \frac{1}{\mathrm{s} - \xi_{\mathrm{L}}}\frac{3\bar{\mathrm{u}}_{\mathrm{N}} - 4\bar{\mathrm{u}}_{\mathrm{N}-1} + \bar{\mathrm{u}}_{\mathrm{N}-2}}{2\Delta\xi} = 0\,, \tag{23}$$

where the velocity value at the center of the ghost cell (i.e.: $\bar{u}_N$) follows by the same extrapolation process used in earlier in equation (20). A similar procedure generates a semi-discrete equation for v_1.

In appendix **??** we present a detailed summary of all the semi–discrete equations used to update each node, cell, and interface (i.e.: s) at the boundary between domains. The numerical scheme is completely defined once we specify how to discretize the time derivatives. This is explained in the next subsection.

6.3 Discretization of the Time Derivatives

In this subsection, following the method of lines approach, we finish the construction of the viscous numerical algorithm. We do so by presenting the strategy used to discretize the time derivatives in the in the semi–discrete equations derived in the earlier subsections. To this end we use the θ-method, which leads to some of the most commonly used (simple) algorithms for time integration.

The semi–discrete equations for the dissipative model can be written in the compact vector ode form

$$\frac{d}{dt}Y = f(Y)\,, \tag{24}$$

where $Y = Y(t)$ is a vector representing the solution to the problem, and f is the nonlinear vector function that follows upon writing the semi–discrete equations in terms of Y. Specifically, we can write Y as a vector having one block of entries per domain, with the blocks separated by the variable giving the position of the corresponding interface s_n. Furthermore, within each block let the Y entries alternate between the node centered specific volume values $\mathrm{v_j}$ and the cell centered flow velocity values $\bar{u}_{j+\frac{1}{2}}$. Note that the values of u in the ghost cells are not included in Y, since they are not evolved in time, and are computed directly by the purely algebraic equations in (20).

Let now $0 \leq \theta \leq 1$ be a relaxation parameter, whose value can be used to control the accuracy and stability of the algorithm (see below). Introduce also a time discretization, with $t_{n+1} = t_n + \Delta t$ and $Y^n = Y(t_n)$. Then the θ-method algorithm for the ode in (24) is given by

$$F(\Delta Y^n, Y^n) = \Delta Y^n - \Delta t\, f\,(Y^n + \theta\, \Delta Y^n) = 0\,, \tag{25}$$

where $\Delta Y^n = Y^{n+1} - Y^n$, and F is defined by the formula. It is well known that: when $\theta \geq 1/2$ this algorithm is unconditionally stable, and when $\theta < 1/2$ the algorithm is conditionally stable only [17]. Particular values of θ give rise to some common time integration strategies:

- $\theta = 0$ gives the explicit forward Euler scheme.
- $\theta = \frac{1}{2}$ gives the second–order, centered implicit trapezoidal rule (or Crank-Nicholson).
- $\theta = 1$ leads to the backwards implicit Euler method.

In our calculations we used a value of θ slightly above 1/2 (in fact $\theta = 0.55$), to assure maximum stability and accuracy.

Given the current state Y^n, equation (25) is a (generally nonlinear) system of equations for the increment vector ΔY^n, which we solve using Newton's method. This requires the calculation of the Jacobian of the nonlinear vector function F, which is a cumbersome but straightforward task — since, in fact, F is made up by fairly simple formulas.

We finally point out that, since the equations used at the interface change as the interface changes type, we monitor where this changes take place, and then adjust the formulas for the function F and its Jacobian accordingly.

6.4 Dissipative Numerical Results

From the analysis in subsection 5.1, it is clear that we should have (at least) three different effective viscosities: one (relatively low) in the austenite ahead of the precursor shock, another (high) one in the critical austenite behind the precursor shock, and a third one in the martensite (behind the phase transformation).

However, the main purpose in introducing dissipation is to explain the broadening of the second rise, after the first sharp one produced by the arrival of the precursor shock, in the free surface experimental velocity plots. It is clear that, for this, the dominant effects will occur in the critical austenite region, as the waves reflected back from the free surface (produced when the precursor shock arrives) propagate into this region and interact with the oncoming phase transformation front. Thus, a *much simplified viscosity–approach is possible: we simply use two values for the viscosity, one (valid everywhere in space) for times before the precursor shock reaches the free surface, and another one for the times after this event.* To be specific: in the equations in (9) we take the effective viscosity μ as a piecewise constant function of time. In this two viscosity model $\mu = \mu_1$ throughout the sample until the precursor shock strikes the free surface. After this collision the value of μ is changed to $\mu = \mu_2$ everywhere in the sample. This simple approach should be able to capture the main changes that the introduction of dissipation causes on the free surface motion.

The numerical experiments we conducted with the dissipative algorithm can thus be described as follows: the code was run with various values of the two viscosities, and (by trial and error) these values were adjusted to have the best fit with the experiments. It is important to point out that **the same two viscosity values were used to simultaneously find the best fit to all the experimental curves**, so that the good fits we obtained (see figure 8) are not merely a consequence of adjusting enough free parameters.

The arguments in subsection 5.1 suggest that the “first” viscosity (the one valid in the sample ahead of the precursor shock) should be low. This is consistent with the experimental results, since this viscosity determines how spread-out the precursor shock is, and the first wave in the experimental plots is very sharp. It is only the second wave that is broad, which agrees with the idea that it is the material behind the precursor shock that is highly dissipative — due to the cracking induced on the crystalline structure by local phase transformations, as explained in subsection 5.1.

The results of our investigation are summarized in figure 8, which shows a remarkably good agreement — given the simplicity of the theory. In fitting the values of the two viscosities, the actual process we used is as follows: we first found the value of the (small) first viscosity, to have the best fit between calculations and experiments for the first wave. Then the value of

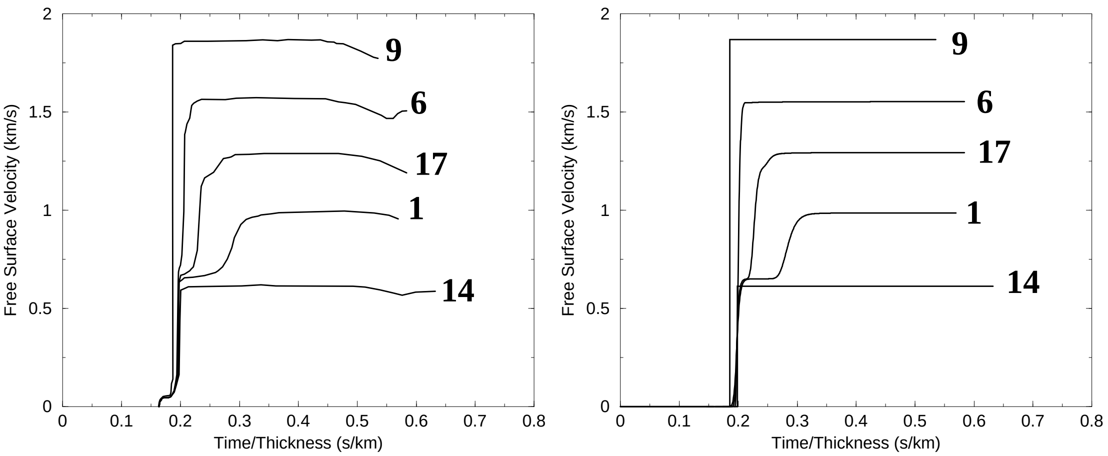

Figure 8: Comparison between the Barker and Hollenbach experiments and the numerical solutions to the two-viscosity model, where the values of the two viscosities (the same for all the curves) are selected to optimize the fit. The actual viscosity values used are given in subsection 6.5.

the (large) second viscosity was found, so as to have the best fit with the second wave. We point out that the results shown are rather insensitive to the value of the first viscosity, in so much that we obtain good agreement with the experiments as long as it is sufficiently small. The sensitivity to the second viscosity is not large either, in so far as small factors (two or three) up and down do not make much of a difference. But the order of magnitude is pinned down with certainty.

6.5 Validity of Viscosity Value

The values of the two effective viscosities leading to the best fit curves shown in figure 8, calculated using the process described in subsection 6.4, are

$$\left.\begin{array}{lllll} \mu_1 & = & 9.11 \times 10^1 \text{ Pa sec} & = & 9.11 \times 10^2 \text{ P}\,, \\ \mu_2 & = & 1.27 \times 10^3 \text{ Pa sec} & = & 1.27 \times 10^4 \text{ P}\,, \end{array}\right\} \tag{26}$$

where the unit used is the CGS unit for dynamic viscosity, the Poise. Note that

$$1P = 1\,\frac{\text{gr}}{\text{cm sec}} = 0.1\,\frac{\text{kgr}}{\text{m sec}} = 0.1\,\text{Pa sec}$$

and that (as a point of comparison), for water under standard conditions: $\mu \approx 10^{-2}$ P. It is also important to note that, while the values above in (26) are the exact ones used to obtain the curves in figure 8, these curves are not very sensitive to the particular values used — as pointed out at the end of subsection 6.4. Thus, the three digits displayed here should not be taken seriously, with the value of μ_1 merely indicating an upper bound on how large the first viscosity can be taken,[1] and the value of μ_2 giving a rough idea (within a factor of two or so) of the appropriate size for the second viscosity.

Obviously, we *can interpret the process leading to* (26) *as that of providing a rough measurement of the effective viscosity — or dissipation coefficient — under the conditions of a large dynamic load produced by the precursor shock in the experiments by Barker and Hollenbach.* The natural question is now: are these numbers reasonable? Is there agreement with other measurements, under similar conditions, to be found in the scientific literature? Clearly, there is no problem with the value of μ_1 we obtained. This value should be interpreted as merely an upper bound on what the two–viscosity model requires for agreement with experiments, and the value is quite consistent with the values viscosity has for most fluids under normal conditions (i.e.: these values do not exceed μ_1 above). The real question has to do with the value of μ_2, which is actually quite large (six orders of magnitude larger than the viscosity of water, for example). We consider this issue next.

Unfortunately, due to the extreme pressures experienced by the sample, direct measurements of the viscosity under these conditions would be very hard, and we were unable to find any within the published literature. The only form of iron under pressures comparable to the ones studies here discussed in the literature, is molten iron in a liquid state. Admittedly, molten iron and solid α or ϵ iron are drastically different phases of the same material. Thus, in any comparison of this sort, the best we can hope to achieve is order of magnitude agreement — which would, at least, give us some extra degree of confidence in the numbers we obtained; or prove us wrong if no agreement occurs.

In molten iron at the high pressures involved, experimental measurements (again) would be very hard, and we found none published. But theoretical calculations have been performed by a number of authors, mostly motivated by geophysical applications. Namely: most of the Earth's core is believed

---

[1] Clearly, with more precise data on the first wave, better values for μ_1 would be easy to obtain.

to be composed of molten iron, at a pressure about 10 times as large as the critical pressure for the α–ϵ phase transformation we have been studying [14]. A determination of the viscosity of the molten core is needed, for example, to explain the damping of radial seismic wave modes propagating in the earth [1]. It is thus *interesting to compare the value of the (second) viscosity* μ_2 *we obtained, with the theoretical predictions from the geophysical literature.*

A thorough literature review of published dynamical viscosity calculations for the Earth's core is presented in [19]. The values reported there for the viscosities in the outer core span 14 orders of magnitude, from 10^{-2} P on the lower end, to 10^{12} P on the upper end. This huge variation is due, in part, to the varying number of ways used to arrive at the values of the parameter, most of which are very indirect (and probably not too reliable). The approaches include (for example) extrapolation from values measured at lower pressures, measurements based on the changes in the Earth's magnetic field over geological time scales, molecular dynamical simulations, and others. The important fact for us, however, is that *the value of* μ_2 *reported in* (26) *is in the middle of this range.*

A second source of measurements, that we can use as a comparison check with our value for the second viscosity, is provided by the measurements of effective viscosities based on shock propagation experiments (without phase transitions) in solids [3, 16, 18, 21]. For example, Band [3] used the approach of comparing the analytic viscous profile for a shock wave with the experimental profile, to obtain a value for the viscosity. Typical values for the viscosities obtained by these approaches are exemplified by the values (for aluminum) given by Prieto et al. [16] at 1.4×10^3 P, and by Sakharov et al. [18] at 2×10^4 P. Both of these values are not too far away from the one for μ_2 in (26) — with a close match not expected, since these shock experiments were done either for materials not exhibiting phase transformations, or with (relatively small) pressure jumps that do not result in a phase transformation.

7 Equation of State Modifications

In this section we consider an alternate physical means by which the Bruno-Vaynblat model could be modified to give more realistic free surface velocity plots, for *impacts in regime B*. As stated above, a modification to the austenite equation of state could be made in hopes of effecting the free surface. When one looks at figure **??** (a) on page **??**, one sees that the width of the reflected fan, W_2^L, is quite narrow. In all of the regime B cases this left-facing rarefaction wave is traveling into a region of austenite at its critical pressure. Along its path this rarefaction fan collides with the phase transformation wave, $W_1^{R,b}$. One of the results of the ensuing interaction is a reflected *composite simple* wave called W_3^R, see subsection **??**. It is this composite wave, that collides with the free surface and affects the free surface velocity plots. In fact when this wave reaches the free surface a second jump in velocity is recorded. Experiments suggest that the second wave should be "smooth", and one speculates that this might happen if the rarefaction wave W_2^L were not so narrow.

As mentioned in section 3, the speed of the head of the leading edge of the W_2^L wave is given by the derivative of the equation of state at the critical pressure of austenite (also see equation (27) of this section). This speed, and therefore the equation of state, plays a very influential role in determining the *thickness* of the reflected fan, W_2^L, and correspondingly the *size* of the interaction region that forms when this rarefaction fan collides with the forward phase transformation. Intuitively the larger the width of this reflected fan the larger the interaction region and therefore the larger the reflected composite simple wave, W_3^R that is sent towards the free surface, see subsection **??** regime B. In contrast to what happens with a Mie-Grüneisen equation of state, if the reflected composite simple wave, W_3^R, is significantly *wide* it might not break before it reaches the free surface and the resulting free surface profile for the second wave would not be so steep, see subsection **??**. If we can prevent shock formation in the W_3^R simple wave we might have a chance at improving the agreement between theory and experiment.

To investigate the effect the austenite equation of state has on the free surface (through the means mentioned above) we modified the equation of state slightly in a neighborhood of the critical pressure p^A_{crit}. The attempt was to *increase* the speed of sound at this point and correspondingly the speed of the head of the reflected rarefaction fan. The speed of sound in an Eulerian coordinate system is given by

$$c^2 = -\mathrm{v}^2 \frac{\mathrm{dp}}{\mathrm{dv}}\,. \qquad (27)$$

From this expression we see that in order to increase the value of the sound speed we need to decrease the value of $p'(\mathrm{v})$ at the critical volume. We note in passing that the definition of the sound speed at *critical* is somewhat ambiguous. Mathematically, it is proportional to $p'(\mathrm{v})$ as in equation (27). For

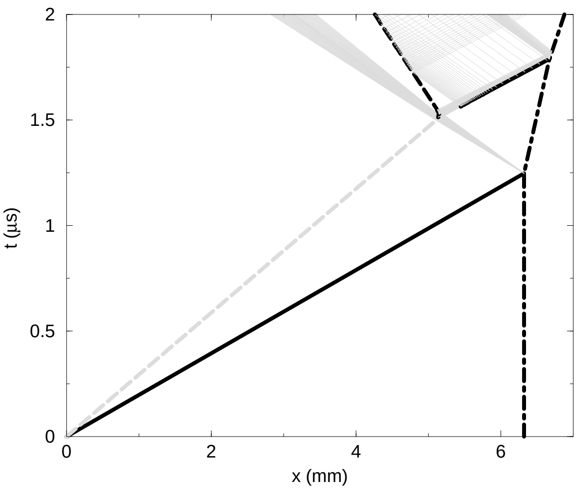

Figure 9: Space time plot of the reflected fan, computed with Mie-Grüneisen equation of state, interacting with the phase transformation wave in a typical regime B situation.

the $p(\mathrm{v})$ relationship used to investigate phase transformations, however, the analytical description of the v-p relationship changes at this critical value, see equation (4). Thus this derivative at critical can only be defined using one-sided limits. Physically the speed of sound should correspond to the speed at which small disturbances, expansive or compressive propagate. When the pressure is critical, however, the material cannot be compressed any further without a phase transformation. To expect this one-sided limit of the slope of the Mie-Grüneisen equation of state to be an accurate representation of the sound speed would be naïve. In fact, the equation of state near the region in which the actual phase transformation takes place is very poorly understood overall. Small modifications to the equation of state in the region near the forward transformation pressure of austenite would certainly be beyond experimental error.

The Mie-Grüneisen equation of state, used in all the sections of this thesis as an equation of state for both austenite and martensite (until now), consisted of the following functional form for the pressure as a function of volume, see appendix **??**

$$p(\mathrm{v}) = \rho_0 \mathrm{a}_0^2 \frac{\eta(\mathrm{v})}{(1 - \mathrm{s}\,\eta(\mathrm{v}))^2}\,. \tag{28}$$

Here ρ_0, a_0, and s are material dependent constants and η is the fractional volume change from some reference state $\tilde{\mathrm{v}}_0$ or

$$\eta(\mathrm{v}) \equiv \frac{\tilde{\mathrm{v}}_0 - \mathrm{v}}{\tilde{\mathrm{v}}_0} = 1 - \frac{\mathrm{v}}{\tilde{\mathrm{v}}_0}\,. \tag{29}$$

The value of $\tilde{\mathrm{v}}_0$ is normally taken to be the specific volume of austenite at zero pressure, or $\tilde{\mathrm{v}}_0 = 1/\rho_0 \equiv \mathrm{v}_0$. We see that $\eta > 0$ corresponds to compression of this volume and $\eta < 0$ corresponds to expansion. The variable η will be used to simplify the presentation whenever possible.

Rather than modify the existing austenite Mie-Grüneisen equation of state given above, we will construct a new one that is not very different from the original. The new equation of state will enable better control over the slope at critical. In constructing this new equation of state for austenite the following, well established criterion, must be satisfied.

1. $p(\mathrm{v}_0) = 0$. The pressure at the rest state for austenite must be zero.
2. $-\mathrm{v}_0^2 \left.\frac{\mathrm{dp}}{\mathrm{dv}}\right|_{\mathrm{v}_0} = \mathrm{c}_0^2$. Here c_0 is the well documented sound speed in austenite at the reference volume v_0.
3. $p(\mathrm{v}_{\mathrm{crit}}) = \mathrm{p}_{\mathrm{crit}}$. The pressure at the *known* critical volume is the *known* critical pressure.
4. $p'(\mathrm{v}) < 0$. The pressure increases with decreasing specific volume.
5. $p''(\mathrm{v}) > 0$. The pressure is a convex function.

These last two criteria are required from purely thermodynamic constraints on the equation of state, see for example [8, p. 5]. While satisfying all of these requirements we would like to be able to make the sound speed at critical as large as possible. The sound speed at critical can be written as

$$c_{\mathrm{crit}}^2 = -\mathrm{v}^2 \left.\frac{\mathrm{dp}}{\mathrm{dv}}\right|_{\mathrm{v}_{\mathrm{crit}}} = \mathrm{v}_0\,(1-\eta)^2 \left.\frac{\mathrm{dp}}{\mathrm{d}\eta}\right|_{\eta_{\mathrm{crit}}}, \tag{30}$$

and an equivalent statement to maximizing c_{crit} is to maximize $\frac{dp}{d\eta}|_{\eta_{\mathrm{crit}}}$. To achieve control over the slope of $p'(\eta)$ at critical, we took a $p = p(\eta)$ equation of state of the following form

$$p(\eta) = a + b\,e^{\eta} + c\,e^{\frac{(\eta-\eta_{\mathrm{crit}})}{\epsilon}}\,. \tag{31}$$

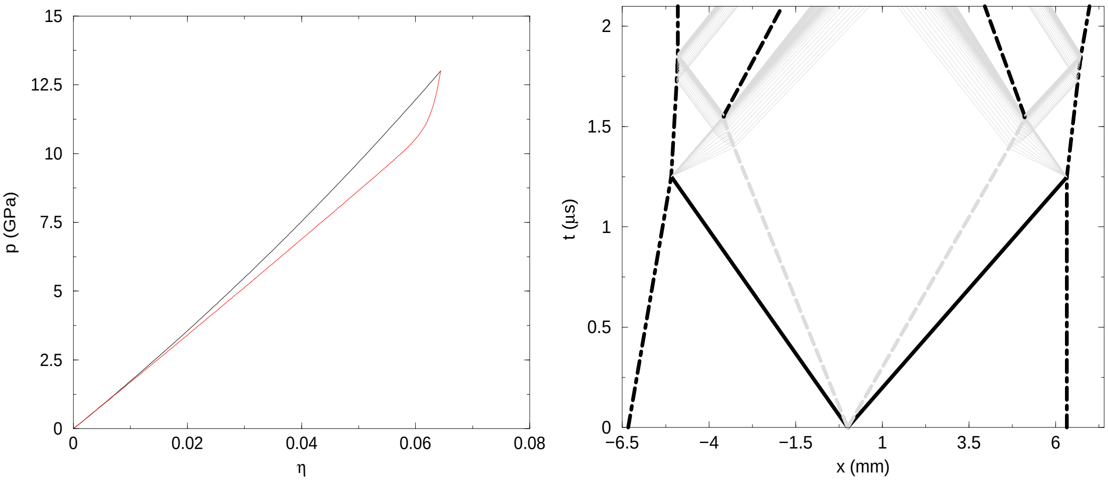

Figure 10: On the left, comparison of the Mie-Grüneisen equation of state with the exponential one proposed in equation (31). On the right, space-time wave diagrams for an impact in regime B for the α–ϵ phase transition in iron, done using the modified equation of state in equation (31).

Requiring conditions 1, 2, and 3 from the above list gives three equations for the three unknowns a, b, and c. These equations can be easily solved. With these three coefficients now determined in terms of known quantities we see that $p'(\eta_{\text{crit}})$ is given by

$$p'(\eta_{\text{crit}}) = b\, e^{\eta} + \frac{c}{\epsilon}\, e^{\frac{(\eta-\eta_{\text{crit}})}{\epsilon}}\Big|_{\eta_{\text{crit}}} = b\, e^{\eta_{\text{crit}}} + \frac{c}{\epsilon}\,, \tag{32}$$

and smaller values of ϵ give larger values of $p'(\eta_{\text{crit}})$ and correspondingly greater values for the sound speed. The value of ϵ is modified to increase the width of the reflected rarefaction fan. The value of ϵ we used in the equation of state is 1.5×10^{-3}.

For comparison, we plot the $p(\eta)$ formula of the austenite Mie-Grüneisen equation of state and equation (31) in figure 10 (left). Notice that the two curves generally agree over a fairly long range of η's but begin to diverge as we approach the critical pressure. We see that the sound speed of the modified equation of state increases greatly over that of the Mie-Grüneisen equation of state at the critical pressure.

In figure 10, we present the (x, t)-diagram, for the first experiment considered by Barker and Hollenbach, see reference [4]. We note that the reflected

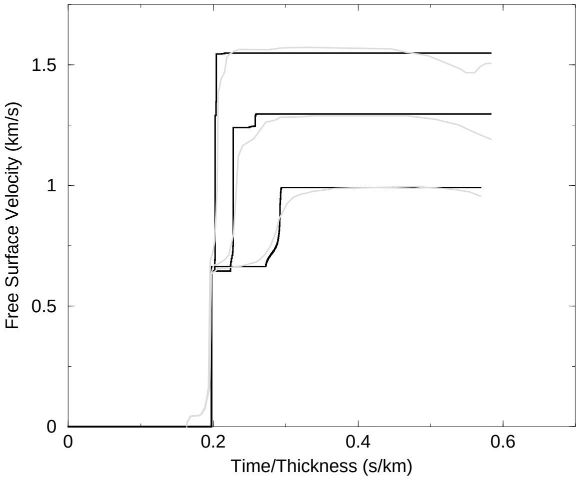

Figure 11: Comparison between Barker and Hollenbach experiments experimental free surface profiles and theoretical free surface profiles predicted from equation (31).

rarefaction fan is indeed much larger when compared with those obtained with the Mie-Grüneisen equation of state (compare with figure **??**). We can also see from this figure that the increase in sound speed brought about by this equation of state does indeed widen the mixed simple wave reflected off the phase transformation, or wave W_3^R. In fact this mixed simple wave is now wide enough that it does not break on its way to the free surface. This in contrast to the behavior predicted to arise from a Mie-Grüneisen equation of state. This indicates that the approach used in this section does indeed have the correct general effect on the behavior, though (as the next paragraph makes clear) it is not enough to provide a complete agreement with the experimental data. More work along this lines is needed, probably incorporating both the ideas hear and the two-viscosity approach used earlier.

In figure 11 one sees the effect the modified equation of state has on three representative free surface plots that correspond to regime B impacts. The interesting result seen here is that the curvature of the theoretical plots near the *beginning* of the second wave matches very well with the experimental ones. The agreement between the two sets of curves in the second wave is not as good for later times. The fact that the agreement between theoretical and experimental curves improved so much in the initial region may be an indication that more investigation into the equation of state near the critical pressure of austenite is warranted.

In the following chapter we present a new numerical scheme developed in the course of working on this problem and used in the presentation of many of the results in this chapter.

References

[1] Don L. Anderson. Bulk attenuation in the earth and viscosity of the core. *Nature*, 285:204–207, 1980.

[2] D. Bancroft, E. L. Peterson, and S. Minshall. Polymorphism of iron at high pressure. *J. Appl. Phys.*, 27:291–298, 1956.

[3] William Band. Studies in the theory of shock propagation in solids. *J. Geophys. Res.*, 65:695–719, 1960.

[4] L. M. Barker and R. E. Hollenbach. Shock wave study of the $\alpha \rightleftarrows \epsilon$ phase transition in iron. *J. Appl. Phys.*, 45:4872–4887, 1974.

[5] J. C. Boettger and D. C. Wallace. Metastability and dynamics of the shock-induced phase transition in iron. *Phys. Rev. B*, 55:2840–2849, 1997.

[6] Oscar Bruno and Dimitri Vaynblat. Shock–induced martensitic phase transitions I: critical stresses, two–wave structures, riemann problems. 2000.

[7] Oscar Bruno and Dimitri Vaynblat. Shock–induced martensitic phase transitions II: Graphite, diamond and iron. 2000.

[8] R. Courant and K. O. Friedrichs. *Supersonic Flow and Shock Waves.* Interscience Publishers, Inc., New York, 1948.

[9] P. S. DeCarli and J. C. Jamieson. Formation of diamond by explosive shock. *Science*, 133:1821–1822, 1961.

[10] D. S. Drumheller. *Introduction to Wave Propagation in Nonlinear Fluids and Solids.* Cambridge University Press, Cambridge, U.K., 1998.

[11] G. E. Duvall and R. A. Graham. Phase transitions under shock-wave loading. *Rev. Mod. Phys.*, 49:523–579, 1977.

[12] D. J. Erskine and W. J. Nellis. Shock–induced martensitic transformation of highly oriented graphite to diamond. *J. Appl. Phys.*, 71:4882–4886, 1992.

[13] James M. Hill. *One–dimensional Stefan Problems: an Introduction.* John Wiley & Sons, Inc., New York, 1987.

[14] R. Jeanloz. Properties of iron at high pressure and the state of the core. *J. Geophys. Res.*, 84:6059–6069, 1979.

[15] J. N. Johnson and L. M. Barker. Dislocation dynamics and steady plastic wave profiles in 6061-T6 aluminum. *J. Appl. Phys.*, 40:4321–4334, 1969.

[16] F. E. Prieto and C. Renero. Steady shock profiles in solids. *J. Appl. Phys.*, 44:4013–4016, 1973.

[17] R. D. Richtmyer. *Difference methods for initial–value problems.* Interscience, New York, 1967.

[18] A. D. Sakharov, R. M. Zaidel, V. N. Mineev, and A. G. Oleinik. Experimental investigation of the stability of shock waves and the mechanical properties of substances at high pressures and temperatures. *Sov. Phys.-Dokl.*, 9:1091–1094, 1965.

[19] R. A. Secco. *Mineral physics and crystallography: a handbook of physical constants.* Wiley–interscience, New York, N.Y., 1995.

[20] J. Smoller. *Shock Waves and Reaction–Diffusion Equations.* Springer, New York, N.Y., 1983.

[21] J. W. Swegle and D. E. Grady. Shock viscosity and the prediction of shock wave rise times. *J. Appl. Phys.*, 58:692–701, 1985.

[22] E. Vlodarchik and R. Trebinski. Transformation of graphite and boron nitride in shock waves. *Shock Waves*, 7:231–248, 1997.

[23] John L. Weatherwax. The characteristic tracking method: A new numerical method for solving 2x2 nonlinear hyperbolic equations. *Undecided*, ??:??, ????

[24] John L. Weatherwax. *Mathematical Modeling of Shock Induced Martensitic Phase Transitions.* PhD dissertation, MIT, Department of Mathematics, Sept 2001.

[25] G. B. Whitham. *Linear and Nonlinear Waves.* Wiley–interscience, New York, N.Y., 1973.